Iron(II) Coordination Complexes with Panchromatic Absorption and Nanosecond Charge-Transfer Excited State Lifetimes

Jason D. Braun, [a] Issiah B. Lozada,[a] Charles Kolodziej,[b] Clemens Burda,[b] Kelly M. E. Newman,[c] Johan van Lierop,[c,d] Rebecca L. Davis[a] and David E. Herbert[a,d]*

[a] Department of Chemistry, University of Manitoba, 144 Dysart Rd, Winnipeg, MB, R3T 2N2, Canada; *david.herbert@umanitoba.ca

[b] Department of Chemistry, Case Western Reserve University, 10900 Euclid Ave, Cleveland, OH, 44106, USA

[c] Department of Physics and Astronomy, University of Manitoba, 31A Sifton Rd, Winnipeg, MB, Canada, R3T 2N2

[d] Manitoba Institute for Materials, University of Manitoba, 20 Sifton Rd, Winnipeg, MB, Canada, R3T 2N2

1   **ABSTRACT**

2   Replacing current benchmark rare-element photosensitizers with ones based on abundant

3   and low-cost metals such as iron would help facilitate the large-scale implementation of

4   solar energy conversion. To do so, the ability to extend the lifetimes of photo-generated

5   excited states of iron complexes is critical. Here, we present a sensitizer design in which

6   iron(II) centres are supported by frameworks containing benzannulated phenanthridine and

7   quinoline heterocycles paired with amido donors. These complexes exhibit panchromatic

8   absorption and nanosecond charge-transfer excited states, enabled by the combination of

9   vacant, energetically accessible heterocycle-based acceptor orbitals and occupied

10   molecular orbitals destabilized by strong mixing between amido nitrogen atoms and iron.

11   This finding shows how ligand design can extend MLCT-type charge-transfer excited state

12   lifetimes of iron(II) complexes into the nanosecond regime and expand the range of

13   potential applications for iron-based photosensitizers.

14

15

16

1   Despite solar energy's potential for mitigating the environmental impacts of

2   powering our planet,[1] the cost of light-harvesting materials still presents a considerable

3   barrier to widespread adoption.[2] In this respect, sensitizing wide band-gap semiconductors

4   by anchoring light-absorbing molecules to their surfaces[3] offers appealing advantages in

5   constructing practical devices from inexpensive, abundant semiconductor materials with

6   low fabrication costs.[4] But designing materials for the global market requires that high-

7   performing sensitizers are also based on abundant and affordable elements.[5] This is

8   likewise true of increasing the sustainability of materials used for solar fuel-forming

9   catalysis[6] and photochemical synthesis.[7] To do so, coordination complexes must ideally be

10   engineered to broadly absorb visible light and exhibit sufficiently long-lived charge-

11   transfer (CT) excited states essential to efficient charge injection[8] or to building up

12   sufficient concentrations of reactive excited states for synthesis.[9]

13   Precious metal photosensitizers tend to fulfill these criteria effectively and

14   photochemical/photovoltaic applications are presently dominated by complexes of Ru and

15   Ir,[10,11] though inventive ligand designs are imbuing complexes of Cu,[11,12] Zr,[13] Co,[14] Cr,[15,16]

16   and W[17] with properties favourable for photosensitizer applications.[18] With respect to

17   abundant and benign metals, iron has long represented a key target in sustainable

18   photosensitizer design.[19] Compared with benchmark precious metal photosensitizers such

19   as $[Ru(bpy)_3]^{2+}$ (bpy = 2,2'-bipyridine), iron coordination complexes typically suffer from

20   rapid, sub-picosecond (ps) relaxation of metal-to-ligand charge transfer (MLCT) states into

21   low-lying metal-centered (MC) states.[20] Strategies to extend CT lifetimes by tuning ligand

22   fields through strengthening metal-ligand bonds have pushed the boundary of accessible

23   charge-transfer excited state lifetimes from ~10 ps[21] to ~20 ps[22] for complexes of strongly

σ-donating cyclometallated carbene[23] or cyanide ligands. This has enabled much higher yields of electron injection into dye-sensitized TiO_2 photoelectrodes compared to those from polypyridyl analogues.[24,25] Further extending this strategy to incorporate six triazolylidene carbenes in an octahedral arrangement about Fe led to a remarkably long-lived ligand-to-metal charge transfer (^{2}LMCT) excited state (~100 ps) and the first example of room-temperature photoluminescence from a low-spin Fe(III) complex[26], with a record ^{3}MLCT lifetime of 528 ps for the reduced Fe(II) analog.[27] Weakening the ligand field by enhancing interligand repulsion can also extend CT excited state lifetimes generated from high-spin ground state Fe(II) compounds, with lifetimes of ~17 ps reported for *bis*-homoleptic Fe(II) complexes of 6,6"-halogenated terpyridines.[28] These design strategies, however, are conceivably limited either by the saturation of an octahedral ligand field with a maximum of six strong σ-donors[29], or the reduced stability of metal-ligand complexes in the weak field limit[28]; neither offers an obvious mechanism for combining extended CT excited state lifetimes and panchromatic absorption.

A distinct design approach is to increase mixing between filled metal t_{2g} orbitals and filled ligand molecular orbitals. Thereby, the character of the highest occupied molecular orbital (HOMO) of an octahedral Fe(II) complex is transformed from being metal-centered to ligand-centered ('HOMO inversion'[30]). This has been predicted computationally to produce dramatic changes in light absorption, including increased molar extinction coefficients and broad absorptive cross-sections across the visible wavelength region.[30] Installing orthogonal, tridentate diarylamido pincer-type ligands on Fe to give octahedral d^6 complexes conceptually fits this design motif: two filled amido N(2p) orbitals would have the appropriate symmetry to mix with orthogonal, occupied

metal d orbitals, resulting in the destabilization of the HOMO and HOMO-1 that would take on anti-bonding (π*(p+d)) character provided orbital energies match and overlap is significant (Figure 1).[31] Combined with moieties that incorporate energetically accessible vacant orbitals elsewhere on the molecular scaffold, such designs should conceivably also exhibit enhanced charge-transfer character in their excited states.[32]

We report that Fe complexes of benzannulated amido pincer-like ligands (Figure 1a) show panchromatic absorption and energetically accessible CT states with well-defined excited state absorption features. Most exciting, these Fe complexes have exceptionally long nanosecond lifetimes that are an order of magnitude longer than previously accessible MLCT lifetimes.[26-29] Our findings expand the available design strategies to produce useful iron-based photosensitizers, successfully addressing the challenges described above.

RESULTS AND DISCUSSION

Synthesis. *Bis*(8-quinolinyl)amido (BQA) ligands are particularly robust examples of chelating diarylamido motifs and pseudo-octahedral iron(II) complexes have been reported;[31] however, poor solubility precluded thorough investigation of their photophysical properties. To remedy this and target improved CT character, we incorporated ancillary substituents and further benzannulation in the form of phenanthridine (3,4-benzoquinoline) units. Compared with quinoline, phenanthridines present more accessible unoccupied orbitals (lower energy, π*-based LUMO) as the dominant resonance contributor is an 'imine-bridged, biphenyl' that maximizes the number of aromatic subunits.[33] The LUMO is thus localized at the C=N, lending phenanthridines

1   conceptually similar electron-accepting character to the prototypical redox non-innocent

2   scaffold (2,6-diimine)pyridine.[34]

3   Following a strategy developed for constructing bidentate analogs[35], we prepared

4   4-halo/4-amino substituted phenanthridines (**1b-c**) and coupled them with 8-

5   aminoquinoline/8-bromoquinoline to access proligands **2a-b** in yields >90% (Figure 2).

6   The formation of **2a-b** was confirmed by multinuclear NMR and in the case of **2a**, single-

7   crystal X-ray diffraction. Addition of base to solutions of either proligand produced a deep

8   purple colour that changed to green on combination with ferrous iron. **3a-b** were isolated

9   as dark green solids following recrystallization. One-electron oxidized species [**3a-b**]$^+$

10   could in turn be isolated as PF_6^- salts via oxidation in air in the presence of $NaPF_6$, or

11   synthesized directly via metallation of **2a-b** with $FeCl_3 \cdot 6H_2O$. Voltammetric analysis of

12   [**3a-b**]PF_6 revealed two additional (quasi)reversible oxidation events (Supplementary

13   Figure 1, Supplementary Table 1) and overlapping reductions below -2 V that are likely

14   phenanthridine-based as similar cathodic events are not observed for the smaller π-system

15   of $Fe(BQA)_2$.[31]

16

17   **Solid-State and Electronic Structures.** The solid-state structures of [**3a-b**]$^{0/+}$ were

18   determined by single-crystal X-ray diffraction (Figure 3a, Supplementary Figure 5). In all

19   four complexes, Fe is in a distorted octahedral geometry with *trans*-disposed amido

20   nitrogens (N_{amido}-Fe-N_{amido} 178-180°; Supplementary Table 2) and drawn-back intraligand

21   N_{phen}–Fe–N_{quin} angles (~166°). While heterocycle $N_{phen/quin}$-Fe bond distances are similar,

22   a slightly shorter distance is observed for each anionic N_{amido}-Fe interaction. Changing the

1   substituent in the 2-position of the phenanthridinyl unit did not significantly impact the

2   coordination environment around Fe.

3   Comparing neutral and cationic compounds, the most pronounced difference is

4   shorter N_{amido}-Fe bonds in [**3a-b**]$^+$ which contracted by an average of 0.04 Å. The $N_{phen/quin}$-

5   Fe distances do not differ significantly. In related pseudo-octahedral complexes of

6   diarylamido ligands, redox-induced changes to N_{amido}-metal distances were found to be

7   sensitive to the degree of mixing between filled metal orbitals and N(2p) lone pairs. For

8   example, there were no significant changes in N_{amido}-metal distances upon oxidation of

9   Ni(II) complexes supported by *bis*(pyrazolyl)amido ligands.[36] Despite the presence of a

10   redox-active Ni(II), the orbital from which oxidation occurred was largely localized on

11   nitrogen with only weak mixing with Ni; the weaker ligand field precluded substantial

12   (p+d) π interactions.

13   In comparison, constriction of the N_{amido}-Fe distance following oxidation of **3a-b** is

14   attributable to depopulation of a HOMO with substantial N-Fe π-antibonding character

15   (Figure 1b). Density functional theory (DFT) calculations reinforce this interpretation. The

16   two highest energy occupied orbitals (HOMO, HOMO-1) of **3a-b** represent π anti-bonding

17   overlap between the amido nitrogens and the metal centre (π*(p+d)). The HOMO-2

18   presents substantial non-bonding character and is localized at iron (~67%). The next two

19   highest energy MOs contain the corresponding π-bonding overlap. Therefore, **3a-b**

20   represent intermediate cases of the 'HOMO inversion' model.[30] Accordingly, the distorted

21   coordination about the Fe ions is clearly identified by the presence of non-zero electric

22   field gradients, quantified by ^{57}Fe Mössbauer spectral doublets for **3a-b** (Supplementary

23   Figure 7) that exhibit much larger splitting (**3a**: quadrupolar splitting Δ = 1.442(1) mm s^{-1}

1   and isomer shift $\delta = 0.2911(6)$ mm s^{-1}; **3b**: $\Delta = 1.425(1)$ mm s^{-1}, $\delta = 0.2863(5)$ mm s^{-1}) than

2   Fe(smif)$_2$[37] ($\Delta = 0.62(1)$ mm s^{-1}, $\delta = 0.30(1)$ mm s^{-1}) that is a neutral pseudo-octahedral

3   Fe(II) complex of tridentate azaallyl ligands (smif = [(2-pyridinyl-CH)$_2$N]$^-$), with *trans*

4   central N donors, flanking pyridyl donors, and very similar N_{py}-Fe-N_{py} bond angles and

5   central N-Fe distances to **3a-b**. Fe(smif)$_2$ is an example of full HOMO inversion, with

6   carbon-based azaallyl HOMO and HOMO-1 MOs that do not significantly mix with Fe-

7   based d-orbitals as a result of the presence of a node at the N bound to Fe.[37] Nor are the

8   isomer shifts and quadrupole splittings as affected by oxidation (i.e., for [**3a-b**]$^{0/+}$) as for

9   other polypyridyl Fe complexes (Supplementary Table 3). Focusing on trends within the

10   two separate pairs of molecules, oxidation of [Fe(terpy)$_2$]$^{2+}$ to [Fe(terpy)$_2$]$^{3+}$,[38] for example,

11   resulted in larger relative changes in δ and Δ compared with [**3a-b**]$^{0/+}$. This suggests that

12   oxidation more strongly perturbs the electronic environment about Fe in [Fe(terpy)$_2$]$^{2+/3+}$

13   compared to [**3a-b**]$^{0/+}$, with a more symmetric electric field about the nucleus in [**3a-b**]$^+$ as

14   evidenced by the significantly smaller values of Δ. Indeed, the EPR spectra of [**3a-b**]PF$_6$

15   collected at 20 K in CH$_2$Cl$_2$ glass contain asymmetric, broad resonances best modeled with

16   slightly inequivalent *g* tensors (Supplementary Figure 8), unlike the rhombic signal

17   observed for [Fe(BQA)$_2$]$^+$.[31] This is inconsistent with localization of the unpaired electron

18   at the metal, though resolved ^{14}N hyperfine coupling was not observed.

19   The lowest energy unoccupied MOs (LUMO, LUMO+1) have limited

20   contributions from Fe and are instead largely comprised of the π^* system of the

21   phenanthridinyl arms (**3a**: LUMO: 77%, LUMO+1: 52%; **3b**: LUMO: 86%, LUMO+1:

22   70%). The quinolinyl π^* systems contribute as well, to a lesser but still significant extent,

23   and more strongly to the LUMO+2 (**3a**: 60%; **3b**: 63%) and LUMO+3 (**3a**: 50%; **3b**: 75%).

1 Exchanging electron-releasing ^{t}Bu groups in **3a** for electron-withdrawing CF_3 substituents

2 in the 2-positions of the phenanthridinyl arms of **3b** increases the phenanthridine

3 contributions to the two lowest energy unoccupied MOs over those from quinoline, slightly

4 stabilizing the LUMO and LUMO+1 and shifting the edge of the lowest energy absorption

5 manifold to lower energy (Figure 3b; calculated HOMO-LUMO gap: **3a** 1.43 eV, **3b** 1.38

6 eV). Indeed, the potential for the reduction of $[\mathbf{3b}]^{0/-}$ (-2.20 V vs $FcH^{0/+}$) is shifted

7 anodically by 230 mV compared to that of $[\mathbf{3a}]^{0/-}$ (-2.43 V), consistent with a lower energy

8 LUMO (DFT-calculated LUMO energies: **3a** -2.20 eV; **3b** -2.40 eV). This substituent

9 effect is mirrored in the first oxidation event, with the $[\mathbf{3a}]^{0/+}$ redox couple accessed at a

10 more negative potential (-0.77 V vs. $FcH^{0/+}$) than $[\mathbf{3b}]^{0/+}$ (-0.61 V). MOs comprised of the

11 remaining two Fe d orbitals that present metal-ligand σ-anti-bonding character (i.e., the e_g

12 states of a symmetric octahedral complex) are significantly destabilized (LUMO+10,

13 LUMO+11). The ligand field of our phenanthridinyl/quinolinyl amido ligands therefore

14 induces considerable N(2p)-Fe(3d) mixing, raising the energy of the two mixed-character

15 HOMOs with the phenanthridinyl moieties dominating the lower energy unoccupied

16 orbital manifolds, and destabilizing metal-centered (MC) excited states in favour of charge-

17 transfer ones.

18 **Steady-State and Transient Absorption (TA) Spectroscopy**. Steady-state UV-Vis

19 spectra showed **3a-b** absorb strongly across the visible spectrum (Figure 3b). The high

20 molar absorptivities (ε ~ 10-30 $mM^{-1}cm^{-1}$) for broad peaks at ~450, 600 and 730 nm that

21 tail off at ~850 nm are consistent with CT character to transitions throughout this region.

22 Time-dependent DFT (TD-DFT) simulations support this assignment. The lowest energy

23 spectral bands (650-900 nm) of **3a-b** are dominated by five key transitions with similar CT

1   character in which electron density is relocated from occupied π^*(p+d) N_{amido}-Fe anti-

2   bonding orbitals (HOMO, HOMO-1) to *N*-heterocycle ligand-based π^* acceptor MOs

3   (LUMO-LUMO+3). These transitions can be described as '$\pi_{anti\text{-}bonding}$-to-ligand charge

4   transfer' (PALCT).[39] Metal-to-ligand charge transfer (MLCT) transitions involving the Fe-

5   localized HOMO-2 occur at higher energy [**3a**: 500-590 nm; **3b**: 556-613 nm] while the

6   corresponding PBLCT ('$\pi_{bonding}$-to-ligand charge transfer') transitions involving the two

7   MOs with π(p+d) N_{amido}-Fe bonding character (HOMO-3, HOMO-4) are found at slightly

8   higher energy (**3a**: 475-510 nm, **3b**: 430-515 nm; Supplementary Tables 8-9). Noting the

9   correlation between the spacing of the first one-electron oxidation and reduction potentials

10   and MLCT energies,[40] the $\Delta E_{1/2}$ calculated for **3a-b** (**3a**: 1.66 V; **3b**: 1.59 V) are ~0.75 V

11   lower than for $[Fe(tpy)_2]^{2+}$ (2.36 V),[41] consistent with the significant red-shift to the lowest

12   energy absorptions of the benzannulated complexes. In the one-electron oxidized

13   complexes ($[$**3a-b**$]PF_6$) most of the absorptive cross-section was attenuated between 600-

14   800 nm, in agreement with the loss of low-energy PALCT transitions. Broad and strong

15   absorptions ($\varepsilon \sim$ 10-20 mM^{-1} cm^{-1}) were evident at ~410 and 510 nm. TD-DFT assigns

16   these bands to CT transitions involving ligand π^* acceptor orbitals (Supplementary Figures

17   26-29 and Tables 12-13). LMCT/$\pi_{anti\text{-}bonding}$-to-metal CT-type transitions involving the

18   singly occupied MO of $[$**3a-b**$]^+$ as the acceptor orbital appear at very low energy ($\lambda_{max} \sim$

19   1000 nm). All features of the steady-state spectra of $[$**3a-b**$]^{0/+}$ were reproduced by

20   spectroelectrochemistry (Supplementary Figure 10).

21   Transient differential pump-probe spectra were collected to investigate the excited

22   state dynamics of **3a-b**. Toluene solutions were excited into the lower energy end of the

23   broad charge-transfer manifold ($\lambda_{excitation}$ = 780 nm) and probed with broadband white light

1 (see SI for complete experimental details). Similar features were observed for both **3a-b**,

2 and so **3b** is described in detail here (see SI for discussion of **3a**). At early delay times of

3 < 1 ps, an excited-state absorption (ESA) band centered at 472 nm was initially observed,

4 followed by a slight red-shift to the ESA and establishment of the ground-state bleach

5 (GSB) which reached maximum intensity at 1.98 ps. The steady-state UV-Vis spectrum

6 shows three main features at wavelengths greater than 400 nm – these are the broad

7 transient bleaching features observed in the time-resolved spectra (Figure 4a). The broad

8 GSB at 600 nm overlapped somewhat with the sharp ESA feature at 485 nm. From 1.98 ps

9 to 3 ns, the ESA broadened slightly, which we attribute to the GSB weakening over this

10 same period.

11   To assign the nature of the excited states responsible for both the ESA and the GSB,

12 we can compare the experimental transient spectra to those of the corresponding oxidized

13 or reduced complexes.[42] The potentials necessary to reduce **3a-b** were quite negative (**3a**:

14 -2.4 V; **3b**: -2.2 V vs FcH$^{0/+}$) and overlapped with a second, irreversible reduction

15 (Supplementary Figure 1). As such, electrochemically generated spectra of the reduced

16 species [**3a-b**]$^-$ could not be obtained. Nevertheless, the oxidized species [**3a-b**]$^+$ presented

17 distinctive optical markers with which charge-transfer states may be distinguished from

18 non-redox, ligand field ones.[42] Notably, the well-defined ESA feature at 485 nm faithfully

19 reproduced an absorption peak observed for [**3b**]$^+$ assigned to PALCT transitions in a

20 region of reduced absorptive cross-section for **3b** (Figure 4a and Supplementary Figures

21 28-29). This feature can confidently be attributed to the redox nature of a charge-transfer

22 state.[28] Similarly, the strong bleach observed between 550-750 nm coincides with the loss

23 of broad, panchromatic absorptive cross-section from **3b** upon oxidation; [**3b**]$^+$ does not

1 absorb at all over this spectral range (Figure 3b). In comparison, the bleach of features

2 close to 450 nm was not as pronounced, indicative of a trade-off in spectral intensity in this

3 region upon oxidation, with the growth of a peak at 416 nm in $[\textbf{3b}]^+$ compensating for

4 reduction of an absorption at 451 nm in **3b**. Experimental limitations prevented acquisition

5 of data in the region of the low energy absorption at 1000 nm.

6 The ESA and GSB fit equally well to single exponent rise and decay functions

7 (Figure 4c). The rise of the ESA was faster than the instrument response time of 150 fs,

8 consistent with the rapid formation of a ^{1}MLCT-like state and subsequent population of a

9 ^{3}MLCT-type one.[43] Intersystem crossing to a ^{3}MLCT state within tens of femtoseconds of

10 population of a ^{1}MLCT state has been established for a range of Fe(II) polypyridyl

11 complexes, including $[Fe(bpy)]_3^{2+}$.[44] Global fit analysis identified two principle

12 components in the TA spectra that resemble the characteristic spectra at 607 fs and 2.71 ps

13 (Figure 4b). An initial ESA was centered at 472 nm at 607 fs without a GSB, and at 2.71

14 ps the ESA has started to decay with the GSB fully established at 600 nm by that time.

15 Decay of both the ESA and bleaching indicates a long-lived CT excited state with a

16 surprising lifetime of > 2 ns for both **3a** and **3b** (Table 1). This is competitive with the

17 longest lived charge-transfer excited states reported for LMCT excited states of Fe(III)

18 complexes[29], and well beyond the MLCT lifetimes of Fe(II) analogues.[27]

19 Changing the solvent had only a small impact on the measured lifetimes, with τ_{decay}

20 reaching 2.7 ns for the ESA feature of **3a** in THF (Supplementary Table 15). Solvent

21 polarity does not appear to play a role in how the compounds relax. As can be seen in the

22 calculated electron-hole maps and natural transition orbitals (NTOs; Supplementary

23 Figures 15-16 and 18-19), a consequence of the symmetry of **3a-b** is that PALCT-type

1 charge-transfer does not reorganize electron density in a strictly linear fashion.

2 Accordingly, large changes in dipole moments are not expected, and there is little solvent

3 dependence to the CT lifetimes.[45]

4 Recent theoretical and experimental work has shown that the excited state

5 landscape of Fe(II) coordination complexes can be complex, as a high density of states and

6 unexpectedly large spin-orbit coupling can enable spin-forbidden channels and render

7 competitive different deactivation pathways.[46,47] In a simplified picture, ^{3}MLCT states of

8 Fe(II) coordination complexes are usually considered to decay via ^{3}MLCT→^{3}MC→^{5}MC

9 pathways,[20] although the extent of participation of the typically highly distorted quintet

10 state can depend on the ligand field.[27] Here, DFT revealed that the lowest-lying metal-

11 centered triplet (^{3}MC) and quintet (^{5}MC) states are destabilized with respect to the ground-

12 state minimum (Supplementary Table 14 and Figure 30). The lowest-lying triplet excited

13 state in the ground state geometry is calculated to have substantial charge-transfer character

14 with diminished spin density at Fe. The increased energies of the lowest-lying MC excited

15 states suggest that the nanosecond CT lifetimes are attributable to an increase in the

16 activation barrier for the decay of the MLCT-type state (here, ^{3}PALCT) to ^{3}MC and lower-

17 lying ^{5}MC states, respectively.

18 Experimentally, the strong ESA features observed in the time-resolved spectra of

19 **3a-b** are also inconsistent with long-lived metal-centered triplets or quintets. ^{3}MC states

20 for Fe systems are typically spectroscopically elusive.[27] Similarly, formation of a metal-

21 centered quintet state tends to result in significant attenuation of optical density ($\Delta\varepsilon \sim 10^3$

22 $M^{-1} cm^{-1}$) as σ-anti-bonding e_g-type orbitals are populated.[48] For example, in $[Fe(terpy)_2]^{2+}$

23 and $[Fe(bpy)_3]^{2+}$ excited-state thermalization increases N-Fe distances by ~0.2 Å which in

1   turn decreases metal-ligand overlap, reducing MLCT peak intensity.[42] For $[Fe(terpy)_2]^{2+}$,

2   the rapid formation and decay of a charge-transfer state into a ligand-field state was also

3   established using TA, with assignment of CT character similarly made by correlating

4   excited state features with electrochemically-generated ones.[42] In that case, the diagnostic

5   marker of a charge-separated species (a reduced terpy⁻ signal) decayed rapidly within the

6   first picosecond of the evolution of the excited state. For **3a-b**, the ESA at 485 nm persisted

7   for nanoseconds.

8   The quintet state predicted by DFT presents long average N-Fe distances compared

9   with the ground state. As a result of this strong distortion, such states do not appear to play

10 a significant role in the decay cascade despite lying at relatively low energy.[47] In

11 comparison, the contraction of N_{amido}-Fe distances in **3a-b** upon oxidation should also be

12 replicated in charge-transfer excited states, maintaining close contacts with the chelating

13 ligands and explaining the intensity of CT peaks observed by TA. This also portends

14 greater photostability. Contrary to ligand-field and fully MLCT excited states (with

15 depopulation of MOs with non-bonding character), metal-ligand interactions in **3a-b**

16 largely strengthen upon excitation as orbitals with anti-bonding character are depopulated.

17 In addition, π-extended phenanthridine based ligands have been shown to increase the

18 rigidity of photoexcited Cu(I) complexes leading to blue-shifted emission compared with

19 smaller quinoline congeners.[49] The exceptionally long, nanosecond excited state CT

20 lifetimes observed for **3a-b** may also benefit from reduced conformational freedom, which

21 could inhibit dynamic processes that lead to intersystem crossing and otherwise faster

22 relaxation.[28]

23 **CONCLUSION**

In summary, we have shown that panchromatic absorption and nanosecond lifetimes of MLCT-type charge-transfer excited states are accessible for coordination complexes of Fe composed of ligands combining HOMO inversion design principles[30] with benzannulated *N*-heterocycle acceptor units (Figure 1). We found that complete inversion of HOMO character from solely metal-based to fully ligand-centered was not critical, but that 'HOMO raising' in combination with judicious acceptor ligand choice can yield low-energy CT states with nanosecond lifetimes. Moreover, an absorption profile with high absorptive cross-section that covers the spectrum from the UV to the edge of the visible (~850 nm) means a greater proportion of the solar spectrum could be harvested with sustainable sensitizers constructed using this ligand design. Furthermore, the MLCT-type nature of the excited state is well-suited for electron injection into n-type semiconductors compared with recently reported Fe(III) complexes with long-lived LMCT excited states.[13,14,26,29] These findings demonstrate how Fe(II) complexes can be constructed to compete with sensitizers based on less abundant[50] or benign metals.[15,16]

METHODS

See Supplementary Information for full details of methods used.

especially grateful to Wenfang Sun and Bingqing Liu for independent verification of preliminary TA data, and to Yurii Zatsikha and Viktor N. Nemykin for assistance setting up spectroelectrochemical experiments and helpful discussions.

DATA AVAILABILITY STATEMENT

All data generated or analysed during this study are included in this published article and its supplementary information files, which include: electrochemical data; UV-Vis and multi-nuclear NMR spectra of all compounds; computational details including comparisons of optimized/crystal structures, TD-DFT results and calculated spectra, extended MO diagrams, population analyses and potential energy surfaces, energies and reaction coordinates; crystallographic information files (CIFs) of **2a**, **3a**, **3b**, [**3a**]PF$_6$ and [**3b**]PF$_6$. Crystallographic data for these structures have also been deposited at the Cambridge Crystallographic Data Centre, under deposition numbers 1589420 (**2a**), 1589421 (**3a**), 1589422 (**3b**), 1589423 ([**3a**]PF$_6$) and 1589424 ([**3b**]PF$_6$). Copies of these data can be obtained free of charge from via www.ccdc.cam.ac.uk/structures. Correspondence and requests for materials should be addressed to D.E.H.

AUTHOR CONTRIBUTIONS

J.D.B. and D.E.H. designed the research. J.D.B., C.K. (transient absorption) and K.M.E.N. (Mössbauer) performed the experiments. K.M.E.N. and J.v.L. provided Mössbauer characterization and analysis. C.K. and C.B. provided TA characterization and analysis. I.B.L. and R.L.D. provided theoretical calculations. J.D.B. and D.E.H. wrote the paper with contributions from all authors.

1

COMPETING INTERESTS

3   The authors declare no competing interests.

4

REFERENCES

1   Lewis, N. S. & Nocera, D. G. Powering the planet: Chemical challenges in solar energy utilization. *Proc. Natl. Acad. Sci.* **103**, 15729-15735 (2006).

2   Haegel, N. M. *et al.* Terawatt-scale photovoltaics: Trajectories and challenges. *Science* **356**, 141-143 (2017).

3   O'Regan, B. & Graetzel, M. A low-cost, high-efficiency solar cell based on dye-sensitized colloidal titanium dioxide films. *Nature* **353**, 737-740 (1991).

4   Hagfeldt, A., Boschloo, G., Sun, L., Kloo, L. & Pettersson, H. Dye-sensitized solar cells. *Chem. Rev.* **110**, 6595-6663 (2010).

5   Bozic-Weber, B., Constable, E. C. & Housecroft, C. E. Light harvesting with Earth abundant d-block metals: Development of sensitizers in dye-sensitized solar cells (DSCs). *Coord. Chem. Rev.* **257**, 3089-3106 (2013).

6   Ardo, S. *et al.* Pathways to electrochemical solar-hydrogen technologies. *Energy Environ. Sci.* **11**, 2768-2783 (2018).

7   Larsen, C. B. & Wenger, O. S. Photoredox catalysis with metal complexes made from earth-abundant elements. *Chem. - Eur. J.* **24**, 2039-2058 (2018).

8   Ponseca, C. S., Chábera, P., Uhlig, J., Persson, P. & Sundström, V. Ultrafast electron dynamics in solar energy conversion. *Chem. Rev.* **117**, 10940-11024 (2017).

9   Schultz, D. M. & Yoon, T. P. Solar synthesis: Prospects in visible light photocatalysis. *Science* **343**, 985 (2014).

10 Robertson, N. Optimizing dyes for dye-sensitized solar cells. *Angew. Chem., Int. Ed.* **45**, 2338-2345 (2006).

11 Prier, C. K., Rankic, D. A. & MacMillan, D. W. C. Visible light photoredox catalysis with transition metal complexes: Applications in organic synthesis. *Chem. Rev.* **113**, 5322-5363 (2013).

12 Housecroft, C. E. & Constable, E. C. The emergence of copper(I)-based dye sensitized solar cells. *Chem. Soc. Rev.* **44**, 8386-8398 (2015).

13 Zhang, Y., Lee, T. S., Petersen, J. L. & Milsmann, C. A zirconium photosensitizer with a long-lived excited state: Mechanistic insight into photoinduced single-electron transfer. *J. Am. Chem. Soc.* **140**, 5934-5947 (2018).

14 Pal, A. K., Li, C., Hanan, G. S. & Zysman-Colman, E. Blue-emissive cobalt(III) complexes and their use in the photocatalytic trifluoromethylation of polycyclic aromatic hydrocarbons. *Angew. Chem., Int. Ed.* **57**, 8027-8031 (2018).

15   Buldt, L. A. & Wenger, O. S. Chromium(0), molybdenum(0), and tungsten(0) isocyanide complexes as luminophores and photosensitizers with long-lived excited states. *Angew. Chem., Int. Ed.* **56**, 5676-5682 (2017).

16   (a) Otto, S. *et al.* [Cr(ddpd)$_2$]$^{3+}$: A Molecular, water-soluble, highly NIR-emissive ruby analogue. *Angew. Chem., Int. Ed.* **54**, 11572-11576 (2015). (b) Jiménez, J.-R., Doistau, B., Besnard, C. & Piguet, C. Versatile heteroleptic bis-terdentate Cr(III) chromophores displaying room temperature millisecond excited state lifetimes. *Chem. Commun.* **54**, 13228-13231 (2018).

17   Sattler, W., Henling, L. M., Winkler, J. R. & Gray, H. B. Bespoke photoreductants: Tungsten arylisocyanides. *J. Am. Chem. Soc.* **137**, 1198-1205 (2015).

18   Wenger, O. S. Photoactive complexes with Earth-abundant metals. *J. Am. Chem. Soc.* **140**, 13522-13533 (2018).

19   Galoppini, E. Light harvesting: Strike while the iron is cold. *Nat. Chem.* **7**, 861-862 (2015).

20   Juban, E. A., Smeigh, A. L., Monat, J. E. & McCusker, J. K. Ultrafast dynamics of ligand-field excited states. *Coord. Chem. Rev.* **250**, 1783-1791 (2006).

21   Liu, Y. *et al.* Towards longer-lived metal-to-ligand charge transfer states of iron(II) complexes: an *N*-heterocyclic carbene approach. *Chem. Commun.* **49**, 6412-6414 (2013).

22   Liu, L. *et al.* A new record excited state ^{3}MLCT lifetime for metalorganic iron(II) complexes. *Phys. Chem. Chem. Phys.* **18**, 12550-12556 (2016).

23   Liu, Y., Wärnmark, K., Liu, Y., Sundstrom, V. & Persson, P. Fe *N*-heterocyclic carbene complexes as promising photosensitizers. *Acc. Chem. Res.* **49**, 1477-1485 (2016).

24   Duchanois, T. *et al.* An Iron-based photosensitizer with extended excited-state lifetime: Photophysical and photovoltaic properties. *Eur. J. Inorg. Chem.* **2015**, 2469-2477 (2015).

25   Harlang, T. C. B. *et al.* Iron sensitizer converts light to electrons with 92% yield. *Nat. Chem.* **7**, 883 (2015).

26   Chábera, P. *et al.* A Low-spin Fe(III) complex with 100-ps ligand-to-metal charge transfer photoluminescence. *Nature* **543**, 695 (2017).

27   Chábera, P. *et al.* Fe(II) hexa *N*-heterocyclic carbene complex with a 528 ps metal-to-ligand charge-transfer excited-state lifetime. *J. Phys. Chem. Lett.* **9**, 459-463 (2018).

28   Fatur, S. M., Shepard, S. G., Higgins, R. F., Shores, M. P. & Damrauer, N. H. A Synthetically tunable system to control MLCT excited-state lifetimes and spin states in iron(II) polypyridines. *J. Am. Chem. Soc.* **139**, 4493-4505 (2017).

29   Kjær, K. S.; *et al.* Luminescence and reactivity of a charge-transfer excited iron complex with nanosecond lifetime. *Science* **363**, 249 (2019).

30   Mukherjee, S., Torres, D. E. & Jakubikova, E. HOMO inversion as a strategy for improving the light-absorption properties of Fe(II) chromophores. *Chem. Sci.* **8**, 8115-8126 (2017).

31   Betley, T. A., Qian, B. A. & Peters, J. C. Group VIII coordination chemistry of a pincer-type bis(8-quinolinyl)amido ligand. *Inorg. Chem.* **47**, 11570-11582 (2008).

32   Mengel, A. K. C. *et al.* A Heteroleptic push-pull substituted iron(II) bis(tridentate) complex with low-energy charge-transfer states. *Chem. - Eur. J.* **21**, 704-714 (2015).

33   Maksić, Z. B., Barić, D. & Müller, T. Clar's sextet rule is a consequence of the σ-electron framework. *J. Phys. Chem. A* **110**, 10135-10147 (2006).

34   Gibson, V. C., Redshaw, C. & Solan, G. A. Bis(imino)pyridines: Surprisingly reactive ligands and a gateway to new families of catalysts. *Chem. Rev.* **107**, 1745-1776 (2007).

35   Mondal, R., Giesbrecht, P. K. & Herbert, D. E. Nickel(II), copper(I) and zinc(II) complexes supported by a (4-diphenylphosphino)phenanthridine ligand. *Polyhedron* **108**, 156-162 (2016).

36   Hewage, J. S. *et al.* Homoleptic nickel(II) complexes of redox-tunable pincer-type ligands. *Inorg. Chem.* **53**, 10070-10084 (2014).

37   Frazier, B. A., Wolczanski, P. T., Lobkovsky, E. B. & Cundari, T. R. Unusual electronic features and reactivity of the dipyridylazaallyl ligand: Characterizations of $(smif)_2M$ [M = Fe, Co, Co^+, Ni; smif = $\{(2\text{-}py)CH\}_2N$] and $[(TMS)_2NFe]_2(smif)_2$. *J. Am. Chem. Soc.* **131**, 3428-3429 (2009).

38   Reiff, W. M., Baker, W. A. & Erickson, N. E. Binuclear, oxygen-bridged complexes of iron(III). New iron(III)-2,2',2''-terpyridine complexes. *J. Am. Chem. Soc.* **90**, 4794-4800 (1968).

39   Dixon, I. M., Khan, S., Alary, F., Boggio-Pasqua, M. & Heully, J. L. Probing the photophysical capability of mono and bis(cyclometallated) Fe(II) polypyridine complexes using inexpensive ground state DFT. *Dalton Trans.* **43**, 15898-15905 (2014).

40   Lever, A. B. P. Electrochemical parametrization of metal complex redox potentials, using the ruthenium(III)/ruthenium(II) couple to generate a ligand electrochemical series. *Inorg. Chem.* **29**, 1271-1285 (1990).

41   Braterman, P. S., Song, J. I. & Peacock, R. D. Electronic absorption spectra of the iron(II) complexes of 2,2'-bipyridine, 2,2'-bipyrimidine, 1,10-phenanthroline, and 2,2':6',2''-terpyridine and their reduction products. *Inorg. Chem.* **31**, 555-559 (1992).

42   Brown, A. M., McCusker, C. E. & McCusker, J. K. Spectroelectrochemical identification of charge-transfer excited states in transition metal-based polypyridyl complexes. *Dalton Trans.* **43**, 17635-17646 (2014).

43   Auböck, G. & Chergui, M. Sub-50-fs photoinduced spin crossover in $[Fe(bpy)_3]^{2+}$. *Nat. Chem.* **7**, 629-633 (2015).

44   Gawelda, W. *et al.* Ultrafast nonadiabatic dynamics of $[Fe^{II}(bpy)_3]^{2+}$ in solution. *J. Am. Chem. Soc.* **129**, 8199-8206 (2007).

45   Lever, A. B. P. *Inorganic Electronic Spectroscopy*. 2nd ed., 208-209 (Elsevier, 1986).

46   Ashley, D. C. & Jakubikova, E. Ironing out the photochemical and spin-crossover behavior of Fe(II) coordination compounds with computational chemistry. *Coord. Chem. Rev.* **337**, 97-111 (2017).

47   Francés-Monerris, A. *et al.* Synthesis and computational study of a pyridylcarbene Fe(II) complex: Unexpected effects of fac/mer isomerism in metal-to-ligand triplet potential energy surfaces. *Inorg. Chem.* **57**, 10431-10441 (2018).

48   Smeigh, A. L., Creelman, M., Mathies, R. A. & McCusker, J. K. Femtosecond time-resolved optical and Raman spectroscopy of photoinduced spin crossover: Temporal resolution of low-to-high spin optical switching. *J. Am. Chem. Soc.* **130**, 14105-14107 (2008).

49   Mondal, R., Lozada, I. B., Davis, R. L., Williams, J. A. G. & Herbert, D. E. Site-selective benzannulation of N-heterocycles in bidentate ligands leads to blue-shifted emission from $[(P^\wedge N)Cu]_2(\mu-X)_2$ dimers. *Inorg. Chem.* **57**, 4966-4978 (2018).

50   Wenger, O. S. Is iron the new ruthenium? *Chem. - Eur. J.* **25**, 6043-6052 (2019).
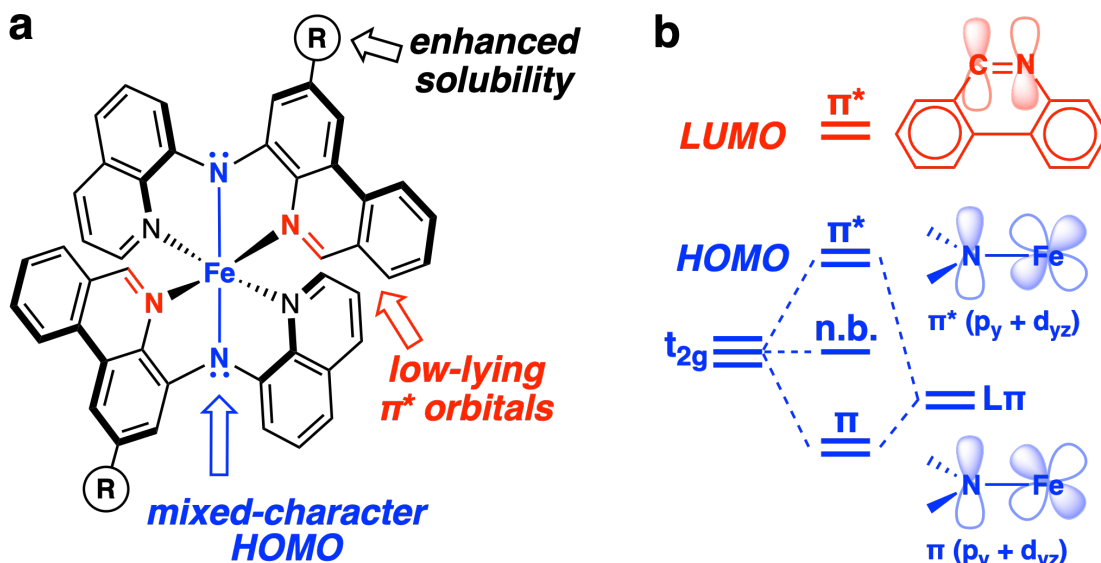
FIGURES

Fig. 1 | Designing pseudo-octahedral iron(II) coordination complexes with pan-chromatic absorption and long-lived charge-transfer excited states. (a) Fe((4-phenanthridinyl)(8-quinolinyl)amido))$_2$ complexes; and (b) schematic showing the design principle in this work: unoccupied phenanthridine-based π^* orbitals and interactions between the t_{2g} orbital set on Fe (using symmetry labels of a fully symmetric octahedral complex) with amido ligand-centered N(2p) orbitals, where significant mixing destabilizes the HOMO, decreasing electron density at Fe.
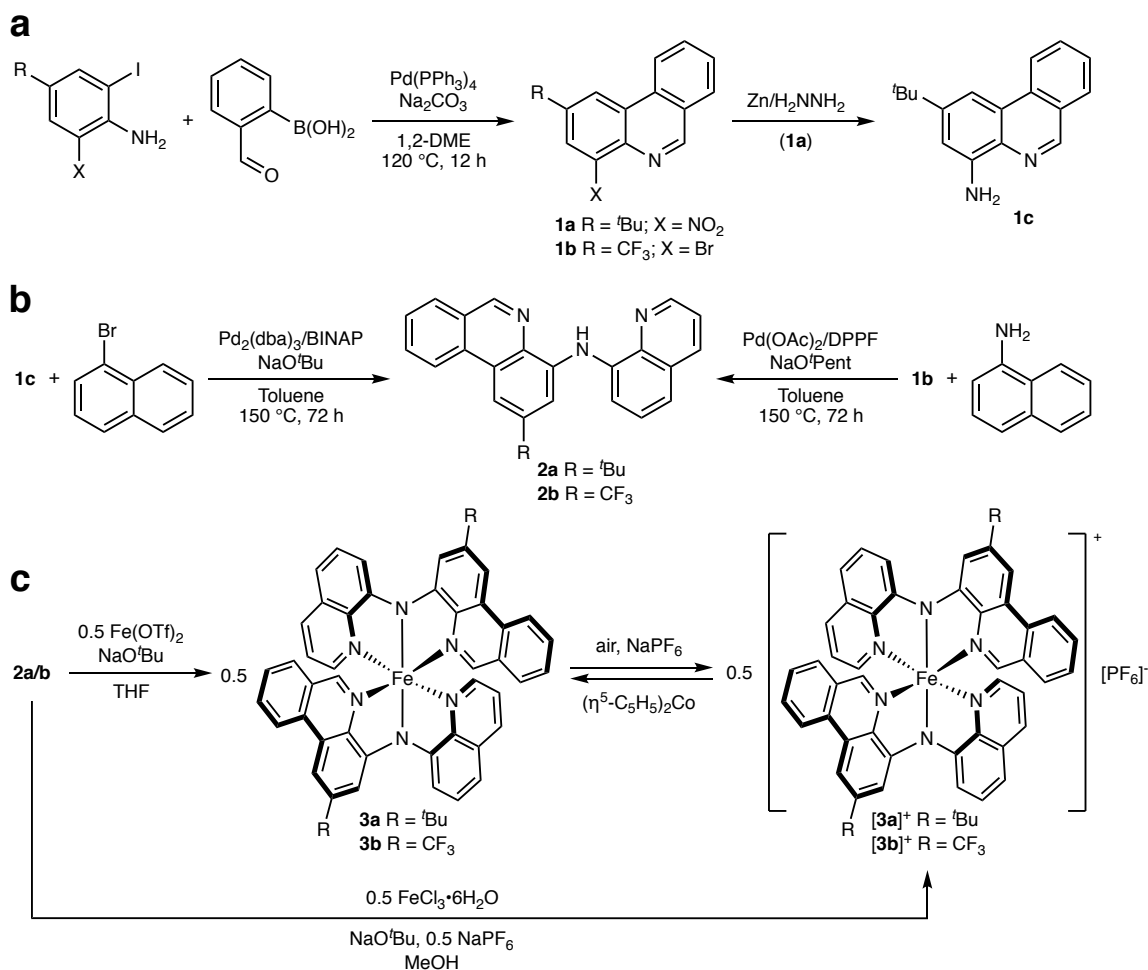
Fig. 2 | Synthesis of (a) 1a-c; (b) proligands 2a-b; and (c) 3a-b/[3a-b]PF₆. Substituted phenanthridine (3,4-benzoquinoline) precursors **1a-c** amenable for elaboration into tridentate ligand scaffolds were constructed via tandem cross-coupling/condensation reactions of appropriately substituted anilines with 2-formylphenylboronic acid. Proligands **2a-b** were assembled by Pd-catalyzed C-N bond forming reactions with either 8-amino- or 8-bromoquinoline, and then installed on Fe(II) or Fe(III) centres to form pseudo-octahedral complexes **3a-b**/[**3a-b**]PF₆. The Fe(II) complexes **3a-b** can be aerobically oxidized by one electron to cleanly give [**3a-b**]⁺, which in turn can be reduced with an appropriate reductant such as cobaltocene [(η⁵-C₅H₅)₂Co].
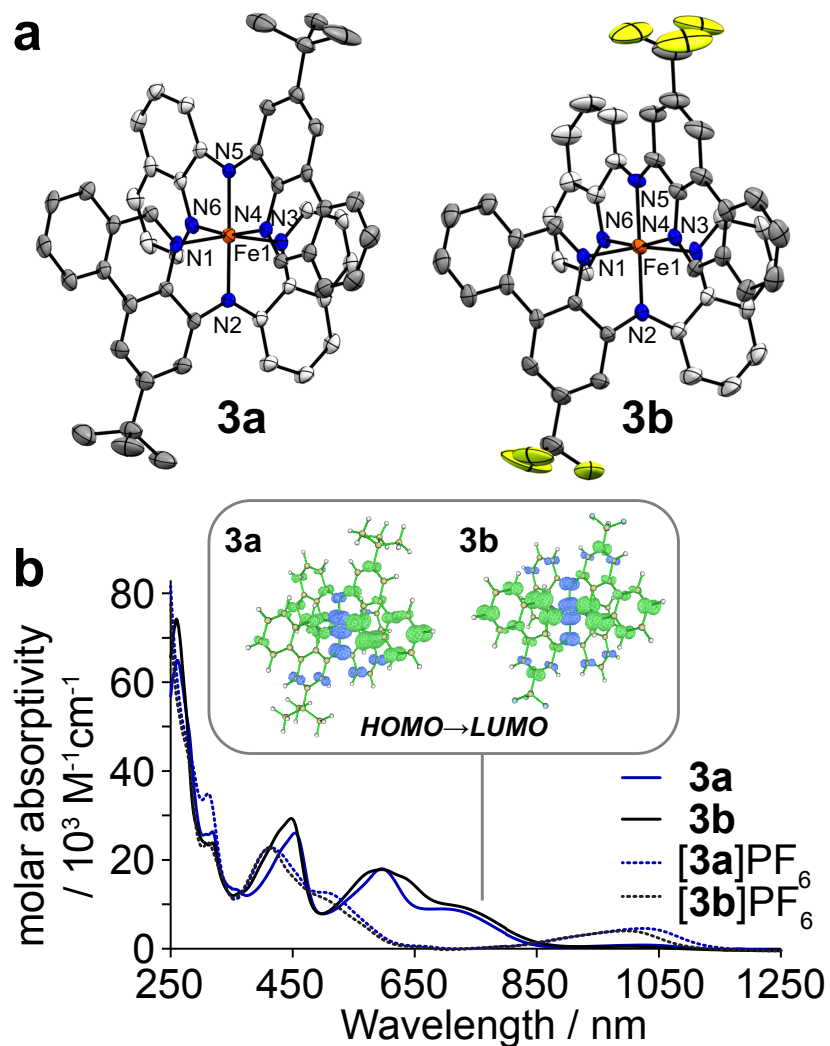
Fig. 3 | Solid-state and electronic structural characterization of 3a-b. (a) Solid-state X-ray diffraction structures of **3a** and **3b**, shown with ellipsoids at 50% probability levels and hydrogen atoms omitted for clarity. The distorted octahedral geometry of each Fe(II) centre is evident, as is the nearly linear arrangement of the *trans*-disposed amido nitrogen centres (N2 and N5) about the metal. Selected bond distances (Å) and angles (°): **3a** Fe1-N1 1.941(3), Fe1-N4 1.945(3), Fe1-N2 1.934(3), Fe1-N5 1.936(3), Fe1-N3 1.943(3), Fe1-N6 1.947(3), N1-Fe1-N3 165.77(12), N4-Fe1-N6 166.11(12), N2-Fe1-N5 179.23(12); **3b** Fe1-N1 1.945(2), Fe1-N4 1.955(2), Fe1-N2 1.924(3), Fe1-N5 1.932(3), Fe1-N3 1.946(2), Fe1-

N6 1.956(2), N1-Fe1-N3 166.46(11), N4-Fe1-N6 165.92(10), N2-Fe1-N5 179.65(11). (b) Steady-state UV-Vis absorption spectra of **3a-b**/[**3a-b**]PF$_6$ in acetonitrile reveal the broad, panchromatic absorption of the Fe(II) complexes. Inset: TD-DFT difference maps [SMD-M06L/6-31+G(d,p)//SMD-O3LYP/6-31+G(d,p)] calculated in acetonitrile showing electron density gain (green) and depletion (blue) distribution maps (isosurface = 0.002). These illustrate the charge-transfer character of the lowest energy transition (HOMO→LUMO) for **3a** and **3b**.
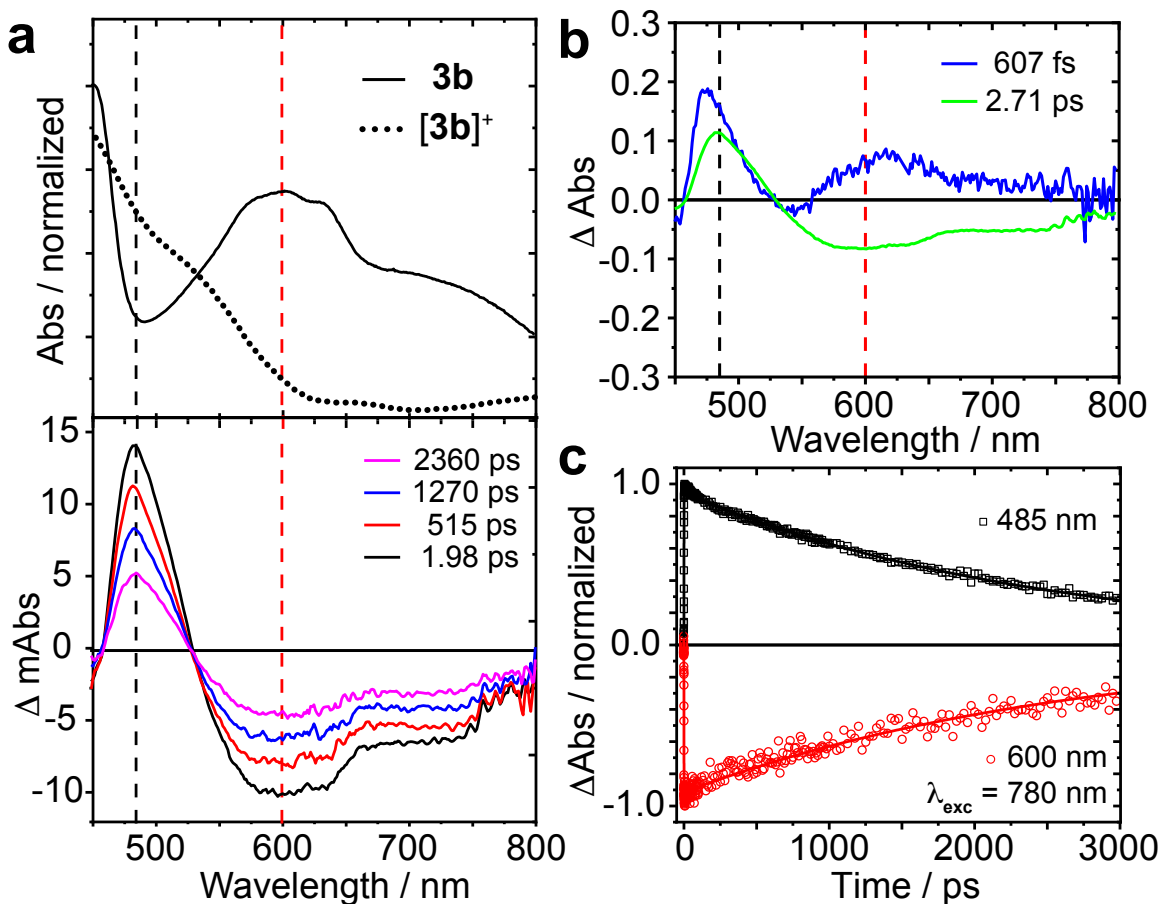
Fig. 4 | Time-resolved absorption spectroscopy and excited state dynamics of 3b (a) Steady-state absorption spectrum of $[\mathbf{3b}]^{0/+}$ (top) and transient absorption spectra (bottom) of **3b** in toluene at indicated time delays. The well-defined excited state absorption feature at 485 nm, which persists for nanoseconds, faithfully reproduces an absorption peak for $[\mathbf{3b}]^+$ (black dashed line) in a region of reduced absorptive cross-section for **3b**. This highlights the charge-transfer nature of the excited state. (b) Global fit analysis principle components constructed from TA data. The two shown components model the main spectral changes: a red shift of the 485 nm absorption and an increase and broadening of the transient bleach at 600 nm. (c) Kinetic traces (see legend) and exponential fits (solid

lines, fitting results are summarized in Table 1) following the decay of both the excited-

state absorption and ground-state bleach at indicated wavelengths.

TABLES

Table 1. Time constants obtained from kinetics traces in toluene shown in Figure 4 and Supplementary Figure 31 at indicated wavelengths, fit to single exponential decay functions.

Compound	λ_{obs} (nm)	τ_{decay} (ps)
3a	486	2041 ± 23
	600	2625 ± 35
3b	485	2454 ± 13
	600	2669 ± 41